Materials Advances

ROYAL SOCIETY OF CHEMISTRY

PAPER

View Article Online
View Journal

Cite this: DOI: 10.1039/d6ma00271d

Unveiling the oxygen adsorption potential of ZIFs: investigating the impact of organic ligands, metal centres, and synthesis methods

Hamidreza Mahdavi, *[ab] Leena Melag,[c] Abdollah Khosravanian,[a] Joydip Mondal, [c] Zongli Xie, *[b] Benny D. Freeman*[ad] and Matthew R. Hill *[e]

Received 26th February 2026,
Accepted 25th March 2026

DOI: 10.1039/d6ma00271d

rsc.li/materials-advances

Zeolitic imidazolate frameworks (ZIFs) have emerged as promising candidates for high O_2 adsorption capacity, O_2/N_2 selectivity and cyclability due to their tunable chemical and structural properties governed by the selection of organic ligands, metal centres and synthesis methods. Therefore, this research engineers ZIF-7, ZIF-8, ZIF-62 and their mixed-metal derivatives containing cobalt (Co) or iron (Fe) (ZIF-8-derived Fe-mIM where applicable) to improve O_2 adsorption. Because performance metrics trade off, no single ZIF maximised all objectives, and application-specific leads were identified. The highest O_2 capacity was delivered by ZIF-8(Zn : Co = 90 : 10)-MS, reaching 0.35 mmol g^{-1} with selectivity of 2.01, and 9.9% decrease over 3 cycles. The greatest selectivity was achieved by ZIF-8-derived Fe-mIM material (Zn : Fe = 0 : 100)-MS, giving selectivity of 2.60 at a low adsorption of 0.09 mmol g^{-1} and 9.6% loss over 3 cycles. The most robust 3-cycle performance was observed for ZIF-8-US, which retained capacity with 0.5% loss while providing 0.26 mmol g^{-1} and selectivity of 1.06. For a balanced generalist over 3 cycles, ZIF-62-US offered the strongest overall combination, providing 0.34 mmol g^{-1}, selectivity of 1.01, and 1.3% loss. These results underscore the delicate balance among O_2 adsorption performance with structural integrity, coordination chemistry, adsorption characteristics, and cyclability in ZIFs shaped by organic ligand, metal centres, and synthesis method choices.

Introduction

Oxygen (O_2) plays a crucial role in various industrial and environmental applications.[1,2] Therefore, the efficient capture, storage, and separation of O_2 from mixed gas streams has attracted significant interest from both academic and industrial sectors.[3–5] The development of advanced adsorbent materials that are capable of selectively adsorbing O_2 has the potential to considerably improve process efficiencies and decrease energy consumption.[6–9] For example, zeolites are scaffolds for gas molecular sieving,[10,11] due to their cost-effective production,[12] exceptional thermal and chemical stability,[13] and ordered microporous structures.[14] However, their rigid frameworks and limited tunability limit their potential.[15,16] Moreover, many zeolites are N_2-selective because N_2 typically interacts more strongly with charged sites than O_2, making O_2-selective adsorption more challenging.[17] These restrictions drive exploration of materials that maintain zeolite-like stability while providing enhanced structural and chemical flexibility.

Zeolitic imidazolate frameworks (ZIFs), a Zn-based subclass of metal–organic frameworks (MOFs), can efficiently integrate the thermal and chemical stability of zeolites with the tunability of MOFs, enabling precise control over pore size, shape, and surface chemistry.[18,19] This tunability arises from flexible organic ligand design and the incorporation of bimetallic centres into the framework *via* various synthesis methods, resulting in versatile structures customised for targeted adsorption and separation applications.[20–26] These characteristics position ZIFs as viable candidates for efficient O_2-selective processes.[27] For example, O_2 adsorption on ZIF-8 shows a distinct gate-opening mechanism, indicating adsorption-induced framework flexibility linked to organic ligand motion.[27] Neutron total scattering combined with Empirical Potential Structure Refinement (EPSR) modelling further indicates that following gate opening, the additional O_2 is mainly accommodated by redistribution towards pore aperture regimes.[28] In another study, multigas (N_2/O_2/Ar/CO) adsorption

[a] Department of Chemical and Biological Engineering, Monash University, Clayton, VIC 3800, Australia. E-mail: benny.freeman@monash.edu, hamidreza.mahdavi1@monash.edu
[b] CSIRO, Manufacturing, Private Bag 10, Clayton South, VIC 3169, Australia. E-mail: zongli.xie@csiro.au
[c] CSIRO, Mineral Resources, Private Bag 10, Clayton South, VIC 3169, Australia
[d] John J. McKetta Jr. Department of Chemical Engineering, The University of Texas at Austin, 2501 Speedway, Austin, TX, 78712, USA. E-mail: benny.freeman@utexas.edu
[e] Department of Materials Science and Engineering, Monash University, Clayton, VIC 3800, Australia. E-mail: matthew.hill@monash.edu

measurements reveal that deformation and multistep adsorption in ZIF-8 are gas-dependent, highlighting the importance of framework flexibility in adsorption behaviour.[29] However, a fundamental question remains: to what extent do organic ligand identity, metal composition, and synthesis method each govern O_2 separation performance?

The organic ligand in ZIFs plays a major role in defining the framework's structure, stability, and adsorption characteristics.[30,31] Organic ligand selection adjusts the pore size, shape, and surface chemistry, thereby regulating O_2–framework interactions and enabling O_2-selective adsorption.[32–36] On the other hand, bimetallic ZIFs introduce synergistic metal–metal interactions that improve adsorption capacity, selectivity, and stability compared to monometallic systems.[37–40] Transition metals with unpaired d-electrons such as cobalt (Co) and iron (Fe), often demonstrate strong O_2 chemisorption that leads to enhanced adsorption and selectivity.[1,36,41] Adjusting the relative metal content provides an extra parameter to optimise performance for certain applications.[42] Finally, the synthesis method controls crystallinity, porosity, and surface chemistry, and thus O_2 adsorption, with each method offering distinct property/scalability trade-offs.[43,44] A variety of synthesis methods are available, including magnetic stirring (MS), overhead stirring (OS),[33,45] ultrasonication (US),[46] a combination of OS and US (OS & US),[45,46] ball milling (BM),[47] and microwave synthesis (MW).[48] Collectively, these three factors (organic ligand, metal, and synthesis) provide a rational design space for optimising O_2 separation in ZIFs.

To date, no systematic comparison has been reported that identifies the individual effects of organic ligand chemistry, mono- *versus* bimetallic centre, and synthesis route while maintaining a constant framework topology within each framework series. Therefore, the field lacks clear guidance on the selection of the optimal composition and scalable strategy that yields the most effective O_2-selective material. This study addresses this gap by elucidating how organic ligand chemistry and metal composition govern O_2 adsorption, selectivity, and cyclability under a controlled synthesis, and evaluating synthesis methods on the best-performing compositions. Additionally, understanding the relationship between material properties and synthesis conditions provides essential insights for the industrial-scale production of ZIFs. Therefore, ZIF-7, ZIF-8, and ZIF-62 synthesised using the MS method were used to investigate the effects of organic ligands and metal centres on O_2 adsorption capacity, selectivity, and structural stability. These three ZIFs exhibit diverse organic ligand chemistries and flexibility/aperture regimes, which serve as a controlled contrast set for assessing the effects of organic ligand identity and framework response on O_2 adsorption, O_2/N_2 selectivity, and cycle stability. This selection was not only based on maximising BET surface area or pre-selecting materials that were known to be the most O_2-selective a priori, but rather on enabling a controlled comparison of ligand identity/flexibility and metal-centre chemistry relevant to O_2/N_2 separation. Additionally, they were selected as widely used benchmark frameworks that are easily synthesised and modified *via* scalable methods. The primary metal ion in all three ZIFs is zinc (Zn), but their organic ligand selection varies. ZIF-7 utilises benzimidazole (bIM), ZIF-8 employs 2-methylimidazole (mIM), and ZIF-62 uses a combination of imidazole (IM) and bIM. Furthermore, mixed-metal derivatives of ZIF-8 incorporating Co and Fe (ZIF-8-derived Fe-mIM where applicable) were investigated, using different molar ratios of Zn : Co and Zn : Fe to assess the influence of bimetallic systems on O_2 adsorption performance. The research extends to bimetallic ZIF-7 and ZIF-62 systems with Zn : Co and Zn : Fe mol% of 90 : 10, and similar assessments were carried out. Finally, to evaluate scalability and processability, a variety of synthesis methods including the MS, OS, US, OS & US, BM, and MW methods were examined on a selected group of candidates.

Experimental

The synthesis of ZIF-7 ($Zn(bIm)_2$), ZIF-8 ($Zn(mIM)_2$), and ZIF-62 ($[Zn(IM)_{2-x}(bIM)_x]$ where $X \approx 0.25$) (Fig. 1a–c) and their bimetallic derivatives with Co and Fe (Fig. 1d and e) was conducted using various synthesis methods, including the MS, OS, US, OS & US, BM, and MW methods (Fig. 1f–k). Initially, the impact of different organic ligands with similar metal centres, then mixed metal centres of varying compositions on crystallinity, porosity, structural integrity, and ultimately, O_2 adsorption performance has been explored. The influence of various synthesis methods on these properties of the chosen samples was studied systematically. The synthesis methods followed the established procedures, as outlined in the SI, Section S2. A comprehensive characterisation was conducted to assess the structural, chemical, thermal, and morphological aspects of

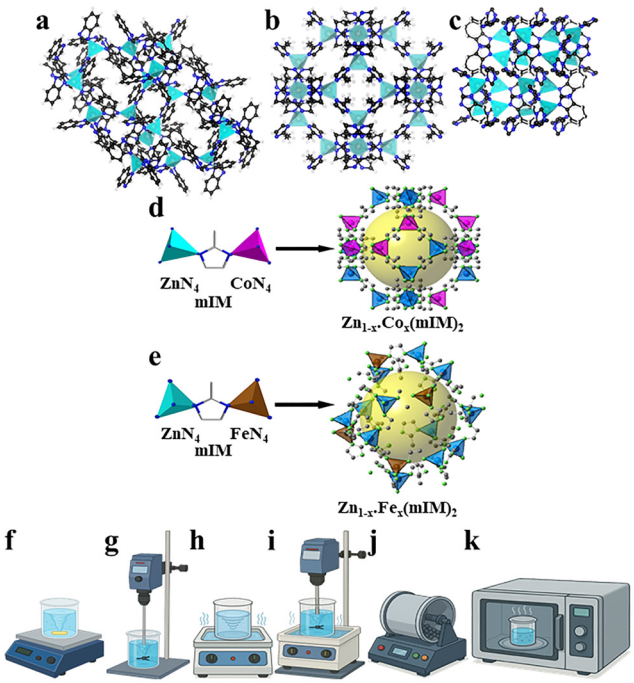

Fig. 1 Structural representations of ZIFs: (a) ZIF-7, (b) ZIF-8, and (c) ZIF-62; schematic structural rearrangements of ZIFs *via* metal substitution: (d) Co incorporation, and (e) Fe incorporation; various synthesis methods of ZIFs: (f) MS, (g) OS, (h) US, (i) OS & US, (j) BM, and (k) MW.

the synthesised materials. The methodologies utilised encompassed powder X-ray diffraction (PXRD) for crystallinity and phase identification, Fourier-transform infrared spectroscopy (FTIR) for evaluating functional group preservation, low-pressure gas adsorption for determining Brunauer–Emmett–Teller (BET) surface areas and pore size distributions (PSDs), thermogravimetric analysis (TGA) for investigating thermal stability, and scanning electron microscopy (SEM) coupled with energy-dispersive X-ray spectroscopy (EDX) for analysing the morphology and elemental composition (see SI, Sections S3–S7 for detailed methodologies and results). Gas adsorption measurements, including O_2 isotherms over multiple cycles, N_2 isotherms, and O_2/N_2 selectivity assessments, were conducted using a Micromeritics 3Flex gas adsorption analyser (see SI, Sections S8 and S9). These investigations resulted in critical insights into the gas adsorption capabilities and selectivity of ZIFs and their bimetallic variations with respect to the organic ligand and metal centre types, mixed metal centres with varied compositions, and different synthesis methods, highlighting their potential for separation applications. The naming convention used in this manuscript is as follows: ZIF-No. (Zn : Co or Fe = x : xx) − y, where No. can be one of 7, 8, or 62; the variable x represents the molar percentage of Zn, xx denotes the molar percentage of Co or Fe, and y indicates the synthesis method. For example, ZIF-8 (Zn : Co = 90 : 10) – MS represents ZIF-8 including 90 mol% Zn and 10 mol% Co synthesised *via* the MS method. In this work, the term ZIF-8 is reserved for samples that retain the characteristic ZIF-8 PXRD reflections; samples that lose long-range order (Fe-rich) are denoted ZIF-8-derived Zn/Fe-mIM materials rather than ZIF-8.

Results and discussion

Effect of organic ligands on O_2 adsorption performance

As illustrated in Fig. 2 (detailed in Fig. S11), the adsorption capacity follows the order of ZIF-62 > ZIF-8 > ZIF-7, whereas O_2/N_2 selectivity follows ZIF-7 > ZIF-8 > ZIF-62 (Table S3). This behaviour primarily highlights how organic ligand chemistry controls pore size, framework flexibility, and host–guest interactions, in addition to surface area.[49] ZIF-62 features a mixed organic ligand composition of imidazole (IM) and bulkier benzimidazole (bIM).[50] This mixed-organic ligand composition exhibits Type-I isotherms with an adsorption-induced gate-opening (narrow-to-expanded-pore) mechanism associated with IM and bIM organic ligands motion and framework distortion,[50] with an average BET surface area and ultramicropore dominated PSD of 7–10 Å (Fig. S5 and Table S1). This is consistent with a balanced rigidity-flexibility that may temporarily expand the effective pore size, thereby increasing accessible pore volume and diffusion pathways.[50] Meanwhile, it preserves confinement and improves O_2–framework interactions without preventing diffusion, because stronger O_2 interactions can promote access to/expansion of the framework and O_2 equilibrates faster than N_2.[50] These factors are consistent with the high O_2 adsorption capacity observed for ZIF-62. Interestingly, ZIF-62 also shows the highest N_2 adsorption capacity likely owing to similar factors of optimal pore size and framework flexibility. Its selectivity of 0.98 (Table S3) which slightly favours N_2, is consistent with the interplay of pore size, kinetic limitations, interaction strength, and molecular sieving.[50] In ZIF-8, gas-induced motion of the mIM organic ligand increases flexibility and pore accessibility,[51] with higher BET surface area and a micropore-dominated PSD of ∼10–16 Å (Fig. S5 and Table S1). Even so, its O_2 adsorption capacity is lower than ZIF-62, probably because the larger pores may reduce confinement-driven O_2–framework interaction strength (*i.e.*, poorer 'fit'), even if diffusion is facilitated.[50,52] Its N_2 adsorption capacity is also lower than ZIF-62, suggesting that the larger pore environment may provide weaker confinement-driven interactions and/or earlier saturation effects for N_2.[49,52] This trend also suggests that pore size and interaction strength matter more than surface area for gas adsorption.[49] The selectivity of 1.07 (Table S3) still reflects a preference for O_2, as slight differences in interaction strength and diffusion kinetics in the flexible framework favour O_2 over N_2.[51] In contrast, ZIF-7 is more aperture-constrained owing to its bulkier bIM organic ligand with phenyl rings and its sorption behaviour is governed by guest-responsive gate-opening driven by organic ligand motion.[53–55] It exhibits a lower BET surface area and a PSD peaked at ∼17–27 Å (Fig. S5 and Table S1) which likely reflects larger PSDs, while gas adsorption remains controlled by a comparatively restrictive pore aperture and a higher gate-opening barrier associated with the bIM organic ligand.[53] As a result, it shows the lowest O_2 adsorption capacity. Similarly, its N_2 adsorption capacity is the lowest, indicating that restricted access (diffusional limitations and higher-pressure gate-opening) limits adsorption under the measurement conditions, despite the larger apparent PSD features.[53] The observed selectivity of 1.42 (Table S3) suggests a stronger preference for O_2, which may reflect differential diffusional/kinetic constraints and/or specific interactions within the narrow-pore form.[53,54]

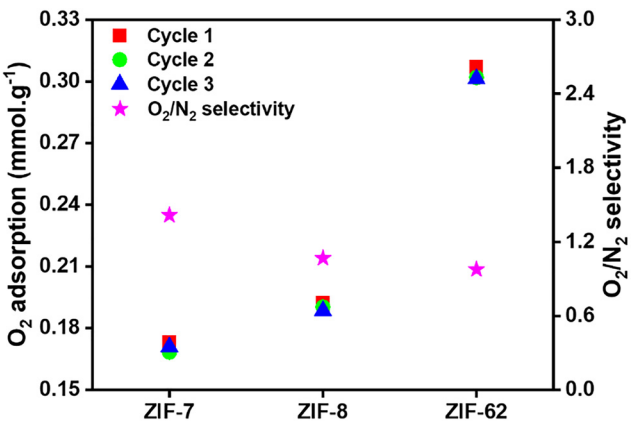

Fig. 2 Effect of organic ligands on O_2 adsorption, O_2/N_2 selectivity, and cyclability of ZIFs, synthesised using the MS method.

Regarding cyclability and structural stability (Fig. 2, detailed in Fig. S15), ZIF-62 and ZIF-8 demonstrate significant stability and consistent adsorption capacity across multiple cycles,

whereas ZIF-7 exhibits a gradual decline in performance. ZIF-62's mixed organic ligands enable an adsorption-induced gate-opening response,[50] with minimal irreversible deformation.[56] This flexibility can help maintain performance despite ZIF-62's comparatively lower surface area.[23,49] Similarly, ZIF-8 adapts to repeated adsorption–desorption cycles due to its framework flexibility arising from mIM-driven organic ligand motions that help maintain pore accessibility.[57,58] In contrast, although ZIF-7 also undergoes gate-opening,[54,55] its transition occurs at higher pressures than ZIF-62,[49] supporting cycling stability for gas adsorption applications.[54] ZIF-7 experiences a decrease in adsorption capacity across cycles which may be associated with the steric constraints of the bIM organic ligand that limit flexibility and structural adaptability and with a less compliant response compared with ZIF-62 under these conditions.[49] This may result in accumulated structural fatigue under cyclic stress. These findings underscore the importance of organic ligand-mediated flexibility of ZIFs in ensuring long-term cycling stability for gas adsorption applications.

Effect of mixed metal centres of varying compositions on O_2 adsorption performance

Incorporating Co or Fe metal ions into the ZIF framework enables isovalent metal substitution that induces structural rearrangements.[59] These rearrangements change the gate-opening energy barrier,[60] pore sizes and interconnectivity,[61] thereby affecting framework stability,[59] and O_2 adsorption capacity.[62] To investigate these effects, ZIF-8 was selected for its moderate O_2 adsorption and selectivity, whereas ZIF-7 demonstrates low adsorption but strong selectivity, and ZIF-62 displays the inverse trend.

The introduction of Co into ZIF-8 at low content (Zn : Co = 90 : 10) significantly improves O_2 adsorption (0.35 mmol g^{-1}) and selectivity (2.01) (Fig. 3a; detailed in Fig. S11a and Table S3). This enhancement is likely associated with Co^{2+}'s partially occupied d-orbitals, which may improve O_2–framework interactions and affect the gate-opening which leads to preferential O_2 adsorption.[41] Moreover, its ionic radius (Co^{2+} = 0.58 Å) and preference for tetrahedral coordination align closely with Zn^{2+} (0.60 Å).[63] Therefore, the ZIF-8 framework experiences minor distortion at low-level substitution as evidenced by retention of the framework with small lattice changes reflected in PXRD peak shifts without phase change (Fig. S1), along with minor FTIR band shifts (Fig. S3) and similar bimodal degradation profiles in TGA with modest shifts across the Co series (Fig. S7). As a result, the structure appears stable, with no clear evidence of major framework disruption at low-level substitution.[59] Thus, the primary cause of the increase in O_2/N_2 selectivity in this regime is the local adsorption environment and changes in adsorption-site chemistry (Co-associated O_2–framework interactions), rather than a change in pore structure. However, as the Co content increases beyond Zn : Co = 90 : 10, both O_2 adsorption and selectivity gradually decrease. At Zn : Co = 0 : 100, these values fall below those of monometallic ZIF-8. This trend suggests that progressive Co incorporation can change the flexibility of the aperture-opening process and

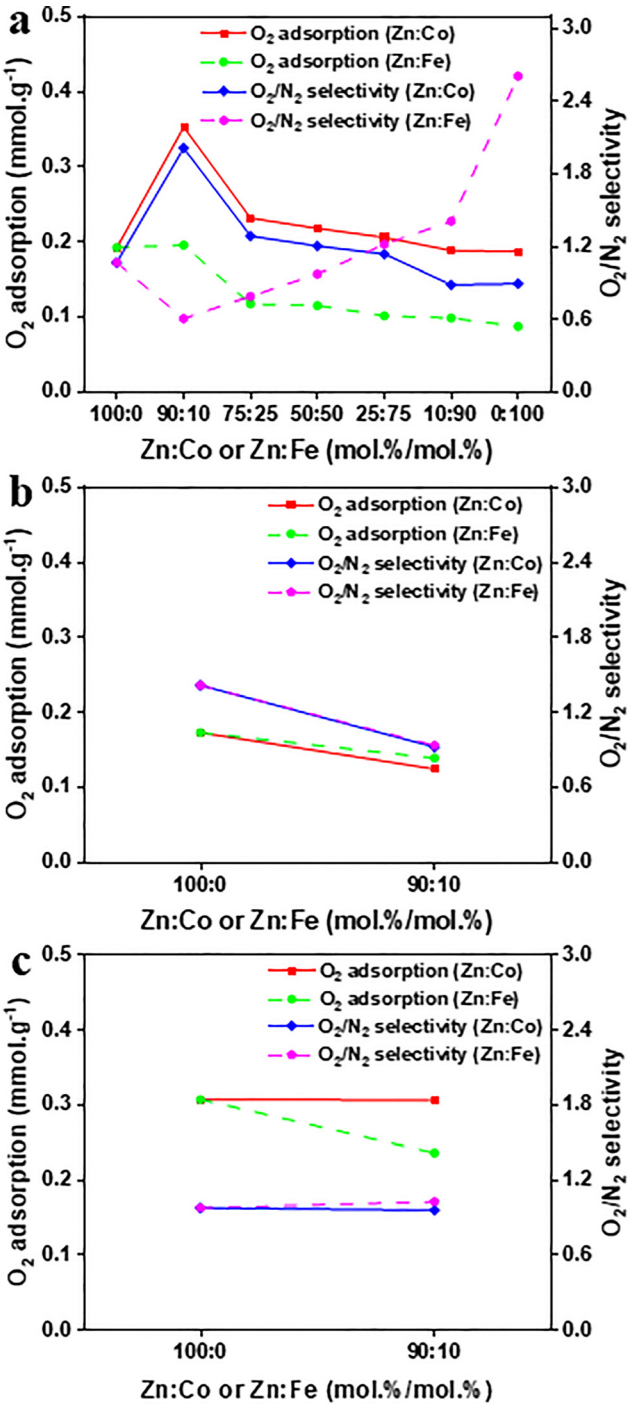

Fig. 3 Effect of mixed metal centres of varying compositions on (a) O_2, N_2, and O_2/N_2 selectivity of ZIF-8 and Zn/Fe-mIM material series, and (b) O_2, N_2, and O_2/N_2 selectivity of ZIF-7 series, and (c) O_2, N_2, and O_2/N_2 selectivity of ZIF-62 series (Zn : Co series shown with solid line; Zn : Fe series shown with dash line), synthesised using the MS method.

may accumulate local distortions that diminish the effective accessibility of pore windows and thereby alter gas–framework interactions.[61] Consequently, the contribution of the most O_2-favourable sites may be diluted and/or less selective adsorption domains may increase, despite the BET surface area rising to 1667 m^2 g^{-1} at Zn : Co mol% of 0 : 100 (Table S1). Because ZIF-8

is flexible, BET surface area derived from N_2 at 77 K does not necessarily represent dynamic pore accessibility at 298 K.[57] Thus, the selectivity trend does not correspond to the BET surface area trend, which means that surface area alone is not the governing descriptor for O_2/N_2 selectivity in the Co series. Simultaneously, N_2 adsorption at a Zn : Co = 90 : 10 is initially lower than ZIF-8, suggesting that minimal Co substitution preferentially enhances O_2 adsorption over N_2, perhaps owing to particular Co-associated O_2–framework interactions (Fig. S13a). At higher Co contents, N_2 adsorption increases and ultimately exceeds ZIF-8, suggesting that structural or chemical modifications enhance the affinity for the more polarizable gas such as N_2,[62] which contributes to the observed reduction in O_2/N_2 selectivity even when overall BET surface area remains high.

Whereas, the introduction of Fe into ZIF-8 at a low content (Zn : Fe = 90 : 10) slightly enhances O_2 adsorption (0.20 mmol g^{-1}) but results in the lowest selectivity (0.61) (Fig. 3a; detailed in Fig. S11b and Table S3). This behaviour may arise from Fe^{2+}'s unpaired d-electrons, which may change O_2–framework interactions and the gate-opening barrier,[36,41] and thus less preferential O_2 binding. Moreover, a slightly larger radius and coordination mismatch (Fe^{2+} = 0.63 Å *versus* Zn^{2+} = 0.60 Å; (Fe^{2+} is more coordination-flexible than Zn^{2+}))[63] that introduces local strain, promotes defect formation, and drives framework distortion even at low substitution levels.[59,61] These defects can introduce additional less-specific adsorption domains that preferentially increase N_2 adsorption relative to O_2, in turn suppressing selectivity at low Fe loading.[64] This is supported by PXRD peak broadening (Fig. S1), a less-faceted particle morphology (Fig. S9), and TGA evidence of earlier mass loss with reduced thermal stability (Fig. S7). As Fe content increases, O_2 adsorption decreases to 0.09 mmol g^{-1} with 9.6% loss in the ZIF-8-derived Fe-mIM material (Zn : Fe = 0 : 100), but selectivity increases to 2.60, indicating its peak value among these samples. Fe substitution, with Fe^{2+} being more coordination-flexible than Zn^{2+}, perturbs the intrinsic tetrahedral Zn-mIM node environment characteristic of ZIF-8, resulting in a significant reduction in BET surface area (Table S1) and compounding strain from the Fe^{2+}/Zn^{2+} size mismatch.[59,65] High Fe contents (ZIF-8-derived Zn/Fe-mIM (Zn : Fe = 75 : 25–0 : 100)) can lose ZIF-8 long-range order and promote significant structural disorder or partial amorphisation, thereby compromising structural stability,[64,66] consistent with the extensive distortion needed to accommodate less compatible Fe nodes.[59,61] While increased Fe distorts the structure and diminishes overall capacity, Fe-centred local chemistry and steric constraints can still favour O_2 over N_2, thereby gradually improving selectivity.[36,67] In the high-Fe regime, the increase in selectivity correlates with the diminished accessible porosity/pore-window restriction (Table S1), which likely restricts N_2 adsorption more than O_2, resulting in a selectivity-capacity trade-off.[36,61] At a Zn : Fe = 90 : 10, N_2 adsorption surpasses monometallic ZIF-8, indicating that early-stage Fe substitution improves overall adsorption capacity, preferentially for N_2 owing to the defects (Fig. S13b). As the Fe content rises, the accumulation of size/coordination mismatch narrows pore size and reduces accessible porosity.[61] This leads to a transition from non-specific defect-assisted adsorption at low Fe to more O_2-selective environments at high Fe, resulting in decreased N_2 adsorption.[61] This trade-off presumably indicates both chemistry and steric changes resulting from framework deformation and partial amorphisation.[66] Simultaneously, the higher selectivity at greater Fe contents supports the idea that partial Fe substitution can enhance specific gas-framework interactions, though overall adsorption capacity declines.

Across the ZIF-8 (Zn : Co) series, all compositions show a gradual reduction in O_2 adsorption over consecutive cycles, likely due to partial pore obstruction or framework degradation. Among them, monometallic ZIF-8 and bimetallic ZIF-8 (Zn : Co = 90 : 10) combine favourable adsorption capacity, selectivity, and cycling stability. This is due to the limited disruption of Zn–organic ligand bonds, which preserves structural integrity (Fig. S15a). The Zn : Fe series shows a similar trend, with each composition exhibiting a slight decline in O_2 adsorption over cycles. However, formulations with low Fe content, such as a Zn : Fe = 90 : 10, attain an effective equilibrium of adsorption and selectivity, coupled with comparatively steady cyclic performance, indicating their suitability for practical applications (Fig. S15b).

To expand the parametric space where functional bimetallic ZIF can be synthesised, the Zn : Co = 90 : 10 and the Zn : Fe = 90 : 10 in ZIF-7 (Fig. 3b), and ZIF-62 (Fig. 3c) were also assessed (detailed in Fig. S11c and d, along with Table S3). The replacement of Zn with either Co or Fe in ZIF-7 lowers both O_2 adsorption and selectivity. This is attributed to the relatively aperture-constrained structure of ZIF-7, which is less capable of accommodating metal substitution, resulting in a lower number of effective O_2 binding sites.[53] Concurrently, the enhanced N_2 adsorption indicates that the modified pore shape generates new pore environments that are more suited to the larger N_2 molecule (Fig. S13c). Both ZIF-7 variations exhibit reduced adsorption beyond the first cycle, suggesting partial pore obstruction or framework deformation induced by metal substitution (Fig. S15c). In ZIF-62, the mixed-organic ligand (IM/bIM) framework tolerates low-level substitution better.[59] ZIF-62 (Zn : Co = 90 : 10) demonstrates a minor decrease in O_2 adsorption with a slight increase in N_2 adsorption which results in reduced selectivity. These trends suggest that Co substitution in ZIF-62 slightly changes the pore environment and weakens O_2 physisorption relative to N_2.[59,61] However, the overall impact remains small due to the flexible framework's ability to dilute local distortions.[59] The Zn : Fe (90 : 10) derivative exhibits a larger drop in both O_2 and N_2 adsorptions, with N_2 decreasing a bit more, leading to a modest increase in selectivity (Fig. S13d). This is ascribed to Fe-induced defects/size-mismatch that constrict windows and reduce accessible porosity, preferentially excluding N_2 over O_2.[59,64] ZIF-62 (Zn : Fe = 90 : 10) has good stability likely due to the flexible framework accommodating Fe-induced strain without catastrophic rearrangement, whereas Zn : Co reveals a gradual decrease in O_2 adsorption, indicative of slow framework deformation or emerging pore obstruction around Co sites (Fig. S15d).

Effect of synthesis methods on O_2 adsorption performance

The impact of various synthesis methods on the structural stability, adsorption capacity, and degradation resistance of ZIFs was assessed by evaluating the changes in adsorption performance over multiple cycles. ZIF-8 and ZIF-62 were selected as monometallic frameworks covering organic ligand flexibility and baseline O_2 capacity, along with ZIF-8 (Zn : Co = 90 : 10) and ZIF-62 (Zn : Fe = 90 : 10) to isolate metal centre effects. Together, these four materials include the extremes in capacity, selectivity, and stability, thereby enabling a sensitive evaluation of how synthesis methods translate O_2 adsorption performance.

The US method achieves the highest initial O_2 adsorption capacity for ZIF-8 at 0.26 mmol g^{-1} (Fig. 4a; detailed in Fig. S12a and S14a, along with Table S4), demonstrating remarkable stability with just a 0.5% decrease over three cycles (Fig. S16a). This exceptional performance likely arises from improved nucleation and more homogeneous dispersion of nuclei under sonochemical conditions,[43] along with cavitation-induced shock waves and microjets that intensify local mixing and mass transfer during coordination formation.[68] US-assisted ZIF syntheses are also widely associated with smaller crystals and narrower PSDs,[46] consistent with the observed PSD (~10–16 Å) and increased surface area (1506 m^2 g^{-1} *vs.* 1402 m^2 g^{-1}), as confirmed by SEM images (Fig. S10) and gas adsorption measurements (Fig. S6 and Table S2). The MS method yields an initial capacity of 0.19 mmol g^{-1} with a slight decline of 2.0%, which suggests good stability, but a lesser capacity compared to the US method. This is consistent with the MS method achieving uniform bulk mixing through a rotating magnetic field, though with weaker shear fields. In contrast, the OS method yields a reduced starting capacity of 0.17 mmol g^{-1} and a more significant 4.7% decline, indicating worse stability relative to MS, likely attributable to less uniform crystallite formation despite intense mixing, good control over shear forces, and dead zones prevention. The OS & US method produces 0.18 mmol g^{-1} but shows a significant 16.1% decline, suggesting a surprising lack of stability that could reflect inadequate synthesis conditions rather than a synergistic effect between the methods. This lack of synergy is expected because intensive agitation can disrupt stable cavitation clouds and redistribute bubbles, resulting in a reduction in local ultrasonic intensity and the formation of generally nonuniform nucleation and growth.[68] The resulting morphological heterogeneity is in accordance with the SEM observations and may result in a lower cyclability than the most effective single-field method. The BM method yields the lowest capacity of 0.13 mmol g^{-1}, reflecting an 10.9% decrease; attributable to high-energy milling inducing defects that undermine the microporous structure.[44,64] This milling-induced disorder, arising from direct mechanical treatment of the precursors, is evidenced by additional and broadened PXRD peaks (Fig. S2a), FTIR band broadening (Fig. S4a), severe BET surface area loss (401 m^2 g^{-1} and Table S2), and a higher low-temperature mass loss (~200 °C; Fig. S8a). These changes reflect the typical BM method trade-off: rapid processing and particle-size reduction at the cost of coordination defects and a partial loss of long-range order,[64,66] which leads to the collapse of N_2-accessible microporosity and an increase of non-selective adsorption domains (Table S2). This results in fewer well-defined micropore adsorption sites for O_2 adsorption are available,[66] leading to decreased O_2/N_2 selectivity (Table S4). The MW method achieves 0.19 mmol g^{-1} with an 7.8% decline, equivalent to the MS method in capacity but exhibiting much worse stability. This is likely owing to rapid heating and fast kinetics that can shift nucleation and growth balance,[69] resulting in defective structures with altered adsorption,[70] as supported by SEM images showing rod-like and less homogeneous crystals (Fig. S10).

For ZIF-8 with a Zn : Co mol% of 90 : 10, framework retention with minor lattice changes is confirmed by PXRD and FTIR (Fig. S2, and S4). The MS method delivers the maximum initial O_2 adsorption capacity of 0.35 mmol g^{-1} (Fig. 4a; detailed in Fig. S12b and S14b, along with Table S4), which may reflect that partial Co substitution can modify adsorption energetics and O_2–framework interactions in ZIF-8.[61,62] The MS method exhibits the highest O_2/N_2 selectivity (Table S4), despite similar surface area and PSD (Table S2). This suggests that method-dependent variations in the effective adsorption landscape, such as Co incorporation uniformity[46] and a reduced

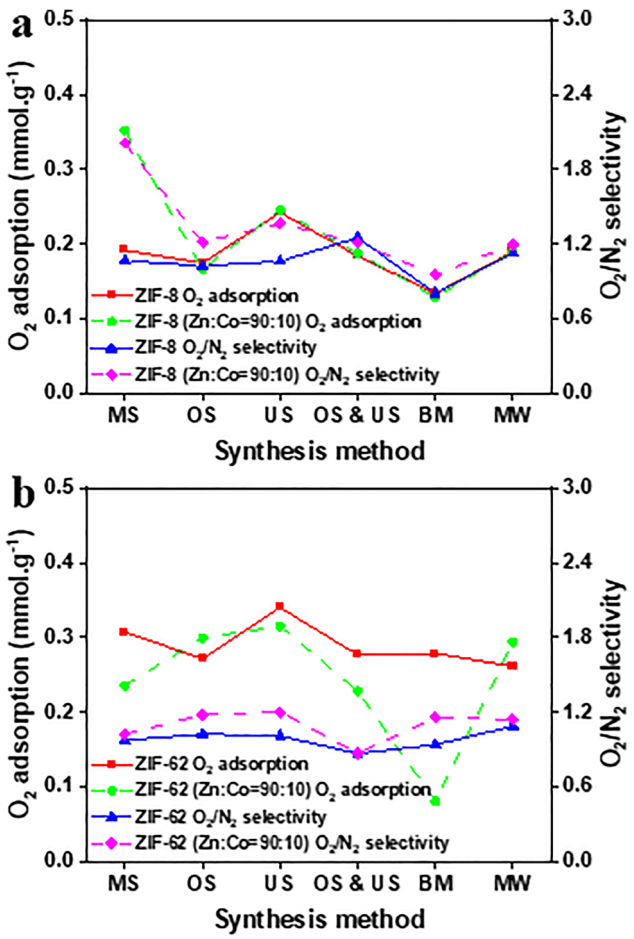

Fig. 4 Effect of synthesis methods on O_2 adsorption, and O_2/N_2 selectivity of (a) ZIF-8, and ZIF-8 (Zn : Co = 90 : 10), along with (b) ZIF-62, and ZIF-62 (Zn : Fe = 90 : 10).

proportion of non-selective defect domains[64] (Fig. S10), rather than surface area, are the primary factors. This maximises the availability of Co-associated O_2-favourable sites while minimising N_2 adsorption. A 9.9% decline across cycles indicates potential instability (Fig. S16b), perhaps due to distortions that reduce pore accessibility. The US method demonstrates a modest capacity of 0.26 mmol g^{-1}, accompanied by a 10.8% decline, suggesting poorer stability than expected. The OS method produces a reduced capacity of 0.17 mmol g^{-1} with a 3.9% decline, indicating better stability than the MS or US methods. The OS & US method yields 0.19 mmol g^{-1} with a 7.5% decrease, demonstrating enhanced stability compared to the MS and US methods, but with lower capacity, as the combined fields can improve reactant dispersion *via* simultaneous acoustic and mechanical effects.[68,69] The MW method reaches 0.19 mmol g^{-1} with only a 1.2% reduction, which implies that rapid crystallisation stabilises the Co-substituted framework. This is consistent with MW's potential for rapid reaction kinetics and potentially more uniform nucleation control.[69] In contrast, the BM method exhibits poor performance at 0.13 mmol g^{-1}, with a significant 34.8% decline, indicative of rapid degradation resulting from mechanical stress. High-energy milling is expected to introduce coordination defects and partially disrupt long-range order,[44,66,71] as reflected by changes in PXRD and FTIR (Fig. S2 and S4) and porosity (Table S2). In the mixed-metal Zn : Co framework, node heterogeneity can further increase local strain, making the material more susceptible to persistent defect formation and pore blockage under the BM method.[59,64] This reduces accessible Co-associated O_2-favourable sites and accelerates capacity degradation (Table S4).

For ZIF-62, method-dependent porosity variations are evident from BET surface area and PSD, while the BM method exhibits defect/secondary-phase signatures in PXRD and FTIR (Fig. S2c and S4c). Across syntheses, TGA indicates relatively similar thermal stability (Fig. S8c). The US method significantly outperforms other methods. It achieves an initial capacity of 0.34 mmol g^{-1} (Fig. 4b; detailed in Fig. S12c and S14c, along with Table S4), and shows a negligible 1.3% decline (Fig. S16c). These results underscore that the US method can intensify mixing, accelerate nucleation, and tune crystal size in ways that improve accessible porosity and reduce performance-limiting heterogeneity.[72] The MS method shows a capacity of 0.31 mmol g^{-1} and a 1.9% decrease, which indicates robust performance in both capacity and stability. The OS method produces 0.27 mmol g^{-1} with a 6.1% reduction, while the OS & US method yields 0.28 mmol g^{-1} with a 3.8% decrease. The MW method yields 0.26 mmol g^{-1} with a 4.7% drop. This intermediate stability is consistent with the MW method generally providing rapid, relatively homogeneous heating and shortened crystallisation kinetics, which can alter defect densities and adsorption outcomes.[69] Although BM introduces defect and secondary-phase signatures in PXRD and FTIR (Fig. S2c and S4c), ZIF-62 maintains a comparable initial O_2 capacity (0.28 mmol g^{-1}). This is likely because milling is followed by a thermal treatment phase that can partially restore the framework connectivity. Indeed, the extent and consequences of disorder are strongly chemistry- and process-dependent.[71] Consequently, any residual defects appear stable over 3 cycles and do not produce measurable capacity loss, and BM does not translate into the same loss of micropore functionality or O_2/N_2 selectivity observed for directly milled frameworks (Tables S2 and S4).

For ZIF-62 with a Zn : Fe mol% of 90 : 10, the US method reaches the highest initial capacity of 0.32 mmol g^{-1} (Fig. 4b; detailed in Fig. S12d and S14d, along with Table S4); however, a 12.6% decline suggests low stability (Fig. S16d). The OS method yields 0.30 mmol g^{-1} with a 16.7% reduction, suggesting that Fe incorporation may increase the framework's sensitivity to local distortions and accessibility losses during cycling, consistent with mixed-metal node effects reported for ZIFs.[59] The MW method yields 0.29 mmol g^{-1} with a 3.6% reduction, achieving a favourable balance between capacity and stability despite a low surface area that underestimates O_2-accessible ultramicroporosity in this flexible structure,[51] presumably owing to the fast and more homogeneous heating that stabilises the Fe-substituted structure.[69] This is consistent with PXRD and FTIR evidence of framework preservation (Fig. S2d and S4d). The MS method yields 0.24 mmol g^{-1} with a 0.9% decrease, which implies increased stability but reduced capacity. The OS & US method yields 0.23 mmol g^{-1}, reflecting a 9.5% decrease, which is modest in every aspect. The BM method yields the lowest capacity (0.08 mmol g^{-1}) and the largest decline (18.0%). For the mixed-metal ZIF-62 (Zn : Fe = 90 : 10), this stronger detrimental impact is consistent with milling-induced disorder reducing accessible porosity and adsorption sites,[64] as well as in mixed-metal ZIF-62, additional heterogeneity at Zn/Fe nodes can amplify local strain,[59] while the Zn–Fe ionic-radius and coordination mismatch can further bias the structure toward persistent disorder and partial pore blockage.[63] that are not fully mitigated during the subsequent thermal treatment phase. As a result, the number of accessible adsorption sites is substantially reduced (Table S2), leading to poor capacity retention (Fig. S16d) and more pronounced defect and secondary-phase signatures in PXRD and FTIR (Fig. S2d and S4d).

Mechanistic framework and design rules

O_2 adsorption performance is governed by a coupled balance between (i) adsorption-site chemistry (metal–O_2 interactions and the availability of O_2-favourable sites), (ii) effective pore accessibility under operating conditions (gate-opening/aperture dynamics and restrictions caused by defects or strain), and (iii) structural integrity under cycling (resistance to irreversible disorder and pore blockage). The dominant contribution depends on the regime: in monometallic ZIFs, flexibility governed by organic ligands and aperture response mainly dictate capacity and cyclability; in bimetallic ZIFs with low substitution, selectivity enhancements are mostly influenced by changes in local site chemistry while maintaining the framework, whereas at higher substitution levels or during defect-prone processing, limitations in accessibility and non-selective domains can dominate, resulting in trade-offs between selectivity and capacity. Synthesis methods modulate these same

factors by controlling crystallinity, defect density, and compositional uniformity, which explains why materials with similar BET surface area and PSD can still exhibit different O_2/N_2 selectivity and stability. To place these design rules in context, a representative literature benchmarking summary of O_2 adsorption, O_2/N_2 selectivity, and recyclability for closely related adsorbents is provided in Table S5.

Among the synthesis methods, the US method improves O_2 adsorption capacity and stability in monometallic ZIFs through optimised nucleation and pore accessibility. Whereas in partial metal-substituted ZIFs, it increased initial capacities, particularly in ZIF-8 (Zn : Co = 90 : 10), but sometimes compromises long-term stability. The MW method demonstrates potential, attaining a robust equilibrium of capacity and stability in bimetallic ZIFs. The OS and OS & US methods provide dependable durability with modest performance, appropriate for long-term operations; however, the OS & US method falls short of expectations in ZIF-8. The BM method shows framework- and protocol-dependent behaviour: direct milling can induce persistent disorder and pore blockage, whereas BM followed by thermal treatment phase (as in ZIF-62) can partially recover framework connectivity, though mixed-metal systems may remain more susceptible to milling-induced heterogeneity. These results highlight the need to customise synthesis methods to particular ZIF compositions to optimise O_2 adsorption and provide insight to develop scalable ZIFs for industrial gas separation and storage.

Conclusions

This study evaluated ZIFs for efficient and sustainable O_2 capture and separation. O_2 adsorption performance in ZIFs is governed by the interplay of organic ligands, metal centres (including secondary metals in bimetallics), and the synthesis method, so a holistic design strategy is required to maximise adsorption capacity, selectivity, and cyclability. In monometallics, gate-opening was enabled by the mixed IM + bIM organic ligand set in ZIF-62 and the highest adsorption was recorded (*e.g.*, 0.34 mmol g^{-1} for ZIF-62 – US), whereas in ZIF-8 with mIM a flexible but slightly larger pore was obtained (moderate adsorption, 0.19 mmol g^{-1} for ZIF-8 – MS), and in ZIF-7 with bIM the more aperture-constrained pores were produced with the highest selectivity of 1.42 at lower capacity. Furthermore, Co^{2+} incorporation into ZIF-8 increased O_2 adsorption and selectivity at low loading (Zn : Co = 90 : 10 – MS: 0.35 mmol g^{-1}; selectivity of 2.01) but a higher 3-cycle loss was incurred (9.9%). Fe^{2+} substitution was shown to reduce capacity at high loading (ZIF-8-derived Fe-mIM material (Zn : Fe = 0 : 100): selectivity 2.60 but 0.09 mmol g^{-1}), yet in ZIF-62 a modest Fe level improved the balance (Zn : Fe = 90 : 10 – MW: 0.29 mmol g^{-1}; selectivity 1.15; 3.6% loss over 3 cycles). Finally, the capacity and cycle stability were generally improved by the US method in monometallics (ZIF-62 – US: 0.34 mmol g^{-1}; selectivity 1.01; 1.3% loss; ZIF-8 – US: 0.26 mmol g^{-1}; selectivity 1.06; 0.5% loss). In bimetallics, stability was better preserved by the MS or MW methods (*e.g.*, ZIF-62 (Zn : Fe = 90 : 10) – MW: 0.29 mmol g^{-1}; selectivity 1.15; 3.6% loss). Therefore, considering balanced performance across three cycles, ZIF-62 – US emerged as the lead candidate. These results clarify the essential roles of organic ligand design, metal substitution, and synthesis optimisation in customising ZIFs for improved O_2 adsorption and separation.

Author contributions

H. M. and L. M. shared co-first authorship, having collaborated closely on the project where they made equal contributions. They jointly led the project administration, conceptual and experimental design, analysis, interpretation of results, and writing the draft. A. K. contributed to the analysis, interpretation of results, and writing the draft, and J. M. contributed to the experimental component of the study. B. D. F. and M. R. H. contributed to the project administration, conceptual and experimental design, analysis, and interpretation of results.

Conflicts of interest

There are no conflicts to declare.

Data availability

The data supporting this article have been included as part of the supplementary information (SI). Supplementary information is available: chemicals, synthesis methods, characterisation methodologies including PXRD, FTIR, low-pressure gas sorption, TGA, and SEM/EDX, along with gas adsorption measurement, and O_2/N_2 selectivity. See DOI: https://doi.org/10.1039/d6ma00271d.

Acknowledgements

The authors acknowledge the use of facilities within the CSIRO Mineral Resources laboratories, Monash, Monash X-ray Platform, and Monash Centre for Electron Microscopy.

References

1 A. L. Sutton, L. Melag, M. M. Sadiq and M. R. Hill, *Angew. Chem., Int. Ed.*, 2022, **61**, e202208305.
2 J. Emsley, *Nature's building blocks: an AZ guide to the elements*, Oxford University Press, USA, 2011.
3 R. J. Allam, *Energy Procedia*, 2009, **1**, 461–470.
4 M. Dobson, *Int. J. Tuberc. Lung Dis.*, 2001, **5**, 520–523.
5 L. Melag, M. M. Sadiq, K. Konstas, F. Zadehahmadi, K. Suzuki and M. R. Hill, *RSC Adv.*, 2020, **10**, 40960–40968.
6 O. Talu, J. Li, R. Kumar, P. M. Mathias, J. D. Moyer Jr and J. M. Schork, *Gas Sep. Purif.*, 1996, **10**, 149–159.
7 N. K. Jensen, T. E. Rufford, G. Watson, D. K. Zhang, K. I. Chan and E. F. May, *J. Chem. Eng. Data*, 2012, **57**, 106–113.

8 J. C. White, P. K. Dutta, K. Shqau and H. Verweij, *Langmuir*, 2010, **26**, 10287–10293.
9 M. Nazari, F. Zadehahmadi, M. M. Sadiq, A. L. Sutton, H. Mahdavi and M. R. Hill, *Commun. Mater.*, 2024, **5**, 170.
10 K. Möller and T. Bein, *Chem. Soc. Rev.*, 2013, **42**, 3689–3707.
11 Y. Li and J. Yu, *Nat. Rev. Mater.*, 2021, **6**, 1156–1174.
12 A. Khaleque, M. M. Alam, M. Hoque, S. Mondal, J. B. Haider, B. Xu, M. A. H. Johir, A. K. Karmakar, J. L. Zhou, M. B. Ahmed and M. A. Moni, *Environ. Adv.*, 2020, **2**, 100019.
13 L. Zhang, K. Chen, B. Chen, J. L. White and D. E. Resasco, *J. Am. Chem. Soc.*, 2015, **137**, 11810–11819.
14 P. Lu, J. Xu, Y. Sun, R. Guillet-Nicolas, T. Willhammar, M. Fahda, E. Dib, B. Wang, Z. Qin, H. Xu, J. Cho, Z. Liu, H. Yu, X. Yang, Q. Lang, S. Mintova, X. Zou and V. Valtchev, *Nature*, 2024, **636**, 368–373.
15 M. Eddaoudi, D. F. Sava, J. F. Eubank, K. Adil and V. Guillerm, *Chem. Soc. Rev.*, 2015, **44**, 228–249.
16 E. Pérez-Botella, S. Valencia and F. Rey, *Chem. Rev.*, 2022, **122**, 17647–17695.
17 H. Demir, S. J. Stoneburner, W. Jeong, D. Ray, X. Zhang, O. K. Farha, C. J. Cramer, J. I. Siepmann and L. Gagliardi, *J. Phys. Chem. C*, 2019, **123**, 12935–12946.
18 D. Zou, D. Liu and J. Zhang, *Energy Environ. Mater.*, 2018, **1**, 209–220.
19 F. S. Butt, A. Lewis, F. Dingwall, N. A. Mazlan, N. Radacsi, X. Fan, X. Chen, Y. Yang, S. Yang and Y. Huang, *Mater. Today Chem.*, 2023, **34**, 101804.
20 K. Noh, J. Lee and J. Kim, *Isr. J. Chem.*, 2018, **58**, 1075–1088.
21 M. A. Nazir, S. Ullah, M. U. Shahid, I. Hossain, T. Najam, M. A. Ismail, A. u Rehman, M. R. Karim and S. S. A. Shah, *Sep. Purif. Technol.*, 2025, **356**, 129828.
22 S. Wang, L. Luo, A. Wu, D. Wang, L. Wang, Y. Jiao and C. Tian, *Coord. Chem. Rev.*, 2024, **498**, 215464.
23 Z. Zheng, Z. Rong, H. L. Nguyen and O. M. Yaghi, *Inorg. Chem.*, 2023, **62**, 20861–20873.
24 S. Sumbal, Z. Aslam, U. Irshad, S. Anwar, A. Abbas, W. Ahmad and A. Hamza, *Appl. Organomet. Chem.*, 2024, **38**, e7747.
25 S. K. Nandigama, V. R. Bheeram and S. B. Mukkamala, *Environ. Chem. Lett.*, 2019, **17**, 447–454.
26 P. Atchutha Rao, H. Padhy, A. Venkateswara Rao, R. Kumar Ganta, S. Bevara, S. Maddila and S. Babu Mukkamala, *Inorg. Chem. Commun.*, 2024, **165**, 112576.
27 B. Russell, J. Villaroel, K. Sapag and A. D. Migone, *J. Phys. Chem. C*, 2014, **118**, 28603–28608.
28 R. Boada, S. Diaz-Moreno, S. E. Norman and D. T. Bowron, *Mol. Phys.*, 2019, **117**, 3456–3463.
29 C. O. Ania, E. García-Pérez, M. Haro, J. J. Gutiérrez-Sevillano, T. Valdés-Solís, J. B. Parra and S. Calero, *J. Phys. Chem. Lett.*, 2012, **3**, 1159–1164.
30 K. S. Park, Z. Ni, A. P. Côté, J. Y. Choi, R. Huang, F. J. Uribe-Romo, H. K. Chae, M. O'Keeffe and O. M. Yaghi, *Proc. Natl. Acad. Sci. U. S. A.*, 2006, **103**, 10186–10191.
31 R. Banerjee, A. Phan, B. Wang, C. Knobler, H. Furukawa, M. O'Keeffe and O. M. Yaghi, *Science*, 2008, **319**, 939–943.
32 A. Phan, C. J. Doonan, F. J. Uribe-Romo, C. B. Knobler, M. O'Keeffe and O. M. Yaghi, *Acc. Chem. Res.*, 2010, **43**, 58–67.
33 H. Mahdavi, H. Zhang, L. K. Macreadie, C. M. Doherty, D. Acharya, S. J. D. Smith, X. Mulet and M. R. Hill, *Nano Res.*, 2022, **15**, 3533–3538.
34 H. Mahdavi, N. T. Eden, C. M. Doherty, D. Acharya, S. J. D. Smith, X. Mulet and M. R. Hill, *ACS Appl. Mater. Interfaces*, 2022, **14**, 23392–23399.
35 R.-B. Lin, S. Xiang, W. Zhou and B. Chen, *Chem*, 2020, **6**, 337–363.
36 D. E. Jaramillo, A. Jaffe, B. E. R. Snyder, A. Smith, E. Taw, R. C. Rohde, M. N. Dods, W. DeSnoo, K. R. Meihaus, T. D. Harris, J. B. Neaton and J. R. Long, *Chem. Sci.*, 2022, **13**, 10216–10237.
37 X. Li, S. Li, J. Liu, J. Zhang, Y. Ren and J. Zhao, *RSC Adv.*, 2024, **14**, 20780–20785.
38 J. Wang, H. Wang, X. Qi, G. Zhi and J. Wang, *Environ. Sci. Pollut. Res.*, 2024, **31**, 32935–32949.
39 K. F. Kayani, *RSC Adv.*, 2024, **14**, 31777–31796.
40 D. Li, A. Yadav, H. Zhou, K. Roy, P. Thanasekaran and C. Lee, *Global Challenges*, 2024, **8**, 2300244.
41 A. S. Rosen, M. R. Mian, T. Islamoglu, H. Chen, O. K. Farha, J. M. Notestein and R. Q. Snurr, *J. Am. Chem. Soc.*, 2020, **142**, 4317–4328.
42 L. Chen, H.-F. Wang, C. Li and Q. Xu, *Chem. Sci.*, 2020, **11**, 5369–5403.
43 B. Chen, Z. Yang, Y. Zhu and Y. Xia, *J. Mater. Chem. A*, 2014, **2**, 16811–16831.
44 P. Kukkar, K.-H. Kim, D. Kukkar and P. Singh, *Coord. Chem. Rev.*, 2021, **446**, 214109.
45 H. Mahdavi, M. M. Sadiq, S. J. D. Smith, X. Mulet and M. R. Hill, *J. Mater. Chem. A*, 2023, **11**, 16846–16853.
46 B. Yao, S.-K. Lua, H.-S. Lim, Q. Zhang, X. Cui, T. J. White, V. P. Ting and Z. Dong, *Microporous Mesoporous Mater.*, 2021, **314**, 110777.
47 S. Al Abdulla, R. Sabouni, M. Ghommem and A. H. Alami, *Heliyon*, 2023, **9**, e21349.
48 F. Hillman, J. M. Zimmerman, S.-M. Paek, M. R. A. Hamid, W. T. Lim and H.-K. Jeong, *J. Mater. Chem. A*, 2017, **5**, 6090–6099.
49 H. Mahdavi, A. Robin, N. T. Eden, A. Khosravanian, M. M. Sadiq, K. Konstas, S. J. D. Smith, X. Mulet and M. R. Hill, *Langmuir*, 2024, **40**, 17387–17395.
50 J. Gandara-Loe, R. Bueno-Perez, A. Missyul, D. Fairen-Jimenez and J. Silvestre-Albero, *ACS Appl. Nano Mater.*, 2021, **4**, 3519–3528.
51 T. Tian, M. T. Wharmby, J. B. Parra, C. O. Ania and D. Fairen-Jimenez, *Dalton Trans.*, 2016, **45**, 6893–6900.
52 C. Zheng, D. Liu, Q. Yang, C. Zhong and J. Mi, *Ind. Eng. Chem. Res.*, 2009, **48**, 10479–10484.
53 T. Xiao and D. Liu, *Mater. Today Energy*, 2019, **14**, 100357.
54 P. Zhao, G. I. Lampronti, G. O. Lloyd, M. T. Wharmby, S. Facq, A. K. Cheetham and S. A. T. Redfern, *Chem. Mater.*, 2014, **26**, 1767–1769.
55 P. Zhao, G. I. Lampronti, G. O. Lloyd, E. Suard and S. A. T. Redfern, *J. Mater. Chem. A*, 2014, **2**, 620–623.
56 J. Song, R. Pallach, L. Frentzel-Beyme, P. Kolodzeiski, G. Kieslich, P. Vervoorts, C. L. Hobday and S. Henke, *Angew. Chem., Int. Ed.*, 2022, **61**, e202117565.

57 D. Fairen-Jimenez, R. Galvelis, A. Torrisi, A. D. Gellan, M. T. Wharmby, P. A. Wright, C. Mellot-Draznieks and T. Düren, *Dalton Trans.*, 2012, **41**, 10752–10762.
58 D. Fairen-Jimenez, S. A. Moggach, M. T. Wharmby, P. A. Wright, S. Parsons and T. Düren, *J. Am. Chem. Soc.*, 2011, **133**, 8900–8902.
59 R. S. Madsen, M. Stepniewska, Y. Yang, A. Qiao, W. M. Winters, C. Zhou, J. König, J. C. Mauro and Y. Yue, *RSC Adv.*, 2022, **12**, 10815–10824.
60 J. G. Vitillo and L. Gagliardi, *Chem. Mater.*, 2021, **33**, 4465–4473.
61 P. Krokidas, S. Moncho, E. N. Brothers, M. Castier and I. G. Economou, *Phys. Chem. Chem. Phys.*, 2018, **20**, 4879–4892.
62 A. Awadallah-F, F. Hillman, S. A. Al-Muhtaseb and H.-K. Jeong, *J. Nanomater.*, 2019, **2019**, 6130152.
63 R. D. Shannon, *Acta Crystallogr., Sect. A*, 1976, **32**, 751–767.
64 I. Bechis, A. F. Sapnik, A. Tarzia, E. H. Wolpert, M. A. Addicoat, D. A. Keen, T. D. Bennett and K. E. Jelfs, *Chem. Mater.*, 2022, **34**, 9042–9054.
65 B. Shen, B. Wang, L. Zhu and L. Jiang, *Nanomaterials*, 2020, **10**, 1636.
66 Q. Ma, H. Jin and Y. Li, *Chem. – Eur. J.*, 2020, **26**, 13137–13141.
67 E. D. Bloch, L. J. Murray, W. L. Queen, S. Chavan, S. N. Maximoff, J. P. Bigi, R. Krishna, V. K. Peterson, F. Grandjean, G. J. Long, B. Smit, S. Bordiga, C. M. Brown and J. R. Long, *J. Am. Chem. Soc.*, 2011, **133**, 14814–14822.
68 D. Meroni, R. Djellabi, M. Ashokkumar, C. L. Bianchi and D. C. Boffito, *Chem. Rev.*, 2022, **122**, 3219–3258.
69 N. A. Khan and S. H. Jhung, *Coord. Chem. Rev.*, 2015, **285**, 11–23.
70 K. Behrens, S. S. Mondal, R. Nöske, I. A. Baburin, S. Leoni, C. Günter, J. Weber and H.-J. Holdt, *Inorg. Chem.*, 2015, **54**, 10073–10080.
71 S. Nikmehr, M. Kazemzad, M. M. Sabzehmeidani, L. Nikzad, T. Ebadzadeh and M. Mousaei, *Results Chem.*, 2023, **5**, 100973.
72 C. Vaitsis, G. Sourkouni and C. Argirusis, *Ultrason. Sonochem.*, 2019, **52**, 106–119.